International Journal of Solids and Structures 164 (2019) 25–36

Contents lists available at ScienceDirect

International Journal of Solids and Structures

journal homepage: www.elsevier.com/locate/ijsolstr

A time-varying mass metamaterial for non-reciprocal wave propagation

Jiahui Huang, Xiaoming Zhou*

Key Laboratory of Dynamics and Control of Flight Vehicle, Ministry of Education and School of Aerospace Engineering, Beijing Institute of Technology, Beijing 100081, China

ARTICLE INFO

Article history:
Received 8 February 2018
Revised 17 November 2018
Available online 28 December 2018

Keywords:
Time-varying mass
Space-time modulation
Non-reciprocity
Unidirectional wave propagation

ABSTRACT

A new type of metamaterial element is proposed to possess time-dependent effective inertial mass, and proved to be valid for the design of the space-time lattice metamaterial that enables non-reciprocal wave propagation. The cell structure is a three-body dynamic system, consisting of a primary body plus two additional bodies that move along the circular orbit. The translational momentum contributed by the orbiting bodies varies periodically depending on their temporal phases, accounting for the time-driven inertial mass observed macroscopically, as verified by the rigorous theoretical derivation. Based on the time-varying mass element, we present the design of the lattice metamaterials with inertial mass that varies periodically in both space and time. Non-reciprocal wave phenomena due to the wave-like modulation of mass are demonstrated by use of the Bloch-based method and the effective-mass representation. The influence of the modulating frequency and amplitude on the asymmetric bandgap is analyzed. The proposed time-varying metamaterial with the non-reciprocal wave behavior is expected to open a new avenue towards unprecedented control over waves and vibrations.

1. Introduction

Reciprocity of wave propagation is a fundamental principle in classical linear-wave systems. It states that the relationship between an oscillating source and the resulting response at a receiver is unchanged if one interchanges the source and the receiver. Non-reciprocal wave propagation, which means the breaking of this form of symmetry (Fink et al., 2000; Miniaci et al., 2017), is becoming desirable because it offers greater possibilities for unprecedented control over waves and vibrations, in applications such as one-way filters and isolation, full-duplex sound communication, etc. (Cummer et al., 2016; Fleury et al., 2015). The non-reciprocity is also of theoretical significance in the context of the symmetry breaking of physical laws under time reversal (Fleury et al., 2015; Zhu et al., 2014). A number of proposals for non-reciprocal wave transportation have been put forward recently. The breaking of reciprocity has been observed in strongly nonlinear mediums with the subharmonic wave generation (Gliozzi et al., 2018; Liang et al., 2010; Liang et al., 2009; Popa and Cummer, 2014), as well as in a pair of gain and loss materials (Gu et al., 2016). It has also been attained by applying the fluid flow to acoustic fields in a way that mimics the Zeeman effect in electromagnetism (Fleury et al., 2014). Another important route to the wave non-reciprocity, which is the interest of this work, is one that relies on the modulated mediums with time-varying material properties.

Composite materials or structures modulated in space are characterized by spatially inhomogeneous material properties. If material parameters are shaped further depending on time, the resulting space-time modulation may form a wave-like field pattern, which behaves as a biasing load that breaks the time-reversal symmetry. In the last century, wave scattering by the space-time modulation has been examined in the context of parametric amplification (Cassedy, 1967; Cassedy and Oliner, 1963; Slater, 1958) and "dynamic materials" (Lurie, 2007). Nowadays, intensive studies are being devoted to the unidirectional wave propagation in spatiotemporal periodic structures (Milton and Mattei, 2017; Nassar et al., 2017a; Shui et al., 2015; Swinteck et al., 2015; Trainiti and Ruzzene, 2016; Vila et al., 2017). Asymmetric bandgaps can be targeted, within which the wave can propagate in only one direction, but would be prohibited in the opposite direction. The modulated materials have also shown an explicit connection with the Willis dynamic mediums (Nassar et al., 2017b); the latter is critical to the control of elastic waves (Milton et al., 2006; Norris and Shuvalov, 2011; Willis, 1981). The specific Willis terms featuring stress-velocity and momentum-strain couplings were found to be relevant to the space-time modulation of material parameters. Exotic wave phenomena, fascinating wave-controlling

* Corresponding author.
E-mail address: zhxming@bit.edu.cn (X. Zhou).

https://doi.org/10.1016/j.ijsolstr.2018.12.029
0020-7683/

devices, and surprising correlations among different physical phenomena can be highly expected from the modulated mediums in future studies. Yet, there is another important issue that needs and deserves great attention, which is the issue of the technological realization of modulated mediums. Recently, rapid developments have been made regarding this challenging problem. The time-varying modulation is potentially feasible by means of programmable piezoelectric components (Casadei et al., 2012; Chen et al., 2016; Chen et al., 2014; Kherraz et al., 2016), shock waves in soft materials (Reed et al., 2003), magneto-rheological elastomers subject to a magnetic field (Danas et al., 2012), the photo-elastic effect (Gump et al., 2004), and so on. These models are most likely responsible for the stiffness modulation. However, it is less apparent how one might create a time-driven inertial mass through these approaches. In this work, we intend to design a completely new, comprehensive, and efficient strategy for the design of time-varying inertial mass.

Inertial mass measures the relationship between the momentum and velocity. In natural materials, it is a positive constant, and not varying over time. Emerging two decades ago, the metamaterial concept offers a new way for making wave functionalities not found in nature, e.g., "negative" mass and/or "negative" modulus. The metamaterials are a special type of composite materials with artificial microstructures (Craster and Guenneau, 2013). From the mechanics point of view, they can be conceptually understood as being "composed of" a group of degrees of freedom (DOFs), in which some are observable, while others can be seen as the hidden. The metamaterial concept is the way that one defines the system dynamics via only the observable DOFs (Bobrovnitskii, 2013; Zhou and Hu, 2009; Zhou et al., 2012). Accordingly, effective material parameters that are redefined in terms of the seen DOFs can account entirely for the effect of the hidden DOFs. It means that, one could design purposely hidden microstructures to acquire targeted properties. For example, introducing the dipole resonance into cell structures has led to the negative inertial mass (Liu et al., 2000). The negative sign of inertial mass discloses the overwhelming effect of out-of-phase inertial motion of the internal DOF (Huang and Sun, 2009; Milton and Willis, 2007; Yao et al., 2008). Metamaterials have also been engineered to have anisotropic inertial density, or the inhomogeneous density in space in order to control the wave trajectory as desired (Christensen et al., 2015; Cummer et al., 2016; Ma and Sheng, 2016; Miniaci et al., 2018; Mousavi et al., 2015). In the present work, we attempt to extend the metamaterial concept to the design of time-dependent inertial mass, which has rarely been explored previously. Past time-invariant metamaterials dictate the common fact that they are "static" without external loadings, so that their effective parameters are irrelevant to the time change. It is intuitively understood that the cell structure of modulated metamaterials should not be at rest even without external loadings if we are to require their inertial mass to vary in time. Following this idea, we have designed a new type of metamaterial element with "dynamic" cell structures, which will be illustrated in Section 2. Effective inertial mass of this new metamaterial will be formulated, which is found to be relevant to the time, yet it still follows the Newton's second law of motion. Deeper physical insight into the time-dependent inertial mass will be also provided. In Section 3, the non-reciprocal wave phenomena will be explored in modulated metamaterials composed of the "dynamic" cells connected each other by springs of constant stiffness. According to the effective-mass representation, the Bloch-based method will be adopted for the dispersion estimation of the space-time lattice metamaterial. The condition for the emergence of asymmetric bandgaps and the effect of modulating parameters will be analyzed by numerical examples. Concluding remarks are outlined in Section 4.

2. Elementary structures with time-varying inertial mass

2.1. Geometry of the model

Consider a rigid body of mass m_0, which is constrained to slide on a one-dimensional motionless track, as shown in Fig. 1. Arranged symmetrically above and below the m_0-body are two sliding tracks, which rotate with a constant angular frequency ω_r. The spinning axis is perpendicular to the motionless track and across the center of the body m_0. The distance between the centers of rotation of the top and bottom tracks is $2d$. Another two rigid bodies of the same mass m_1 are placed on the rotating tracks; one is located on the top and the other on the opposite side of the bottom. They are pin-connected to the primary body m_0 by rigid and massless bars of length l. Ensure that the direction of gravity coincides with the spinning axis, so that the gravitational force of all bodies need not be taken into account in our analysis.

To describe the motion of the three rigid bodies, we introduce two coordinate systems: a fixed inertial system of coordinates [X, Y, Z], and a moving system of plane coordinates (x, y). In the fixed system, the X axis is set along the motionless track and the Z axis coincides with the spinning axis. At time t, the m_0-body, when subject to an external force $F(t)$, is located at [$U_0(t)$, 0, 0], where $U_0(t)$ is its displacement, satisfying $U_0(t=0)=0$. Unit vectors $\mathbf{e}_x$ and $\mathbf{e}_y$ for the moving system (x, y) are set along and perpendicularly to the rotating tracks respectively, and the center of rotation is taken as the coordinate origin. Coordinates of the orbiting masses can be expressed as (r_T, 0) and (-r_B, 0) in the moving system, where r_T and r_B stand for their distances to the origin. Without loss of generality, we assume that the x and y axes coincide with the X and Y axes at the initial time $t=0$. In this scenario, the coordinates of orbiting bodies in the fixed system can be expressed as $[r_\mathrm{T}\cos(\omega_\mathrm{r}t), r_\mathrm{T}\sin(\omega_\mathrm{r}t), d]$ and $[-r_\mathrm{B}\cos(\omega_\mathrm{r}t), -r_\mathrm{B}\sin(\omega_\mathrm{r}t), -d]$.

2.2. Definition of effective time-varying inertial mass

Under an arbitrary external force F, the m_0-body undergoes the displacement U_0, which is relevant to the complex interaction among bodies. Our strategy is to derive theoretically the explicit relation between F and U_0 by considering orbiting bodies as the hidden microstructure. The analytic expression of effective mass $m_\mathrm{eff}(t)$ can then be retrieved by casting the relation into the form of Newton's equation $F = \mathrm{d}[m_\mathrm{eff}(t)\dot{U}_0]/\mathrm{d}t$. Following this concept, we begin with the equilibrium equation of the m_0-body

$$F - F_\mathrm{T}\frac{r_\mathrm{T}\cos(\omega_\mathrm{r}t) - U_0}{l} - F_\mathrm{B}\frac{r_\mathrm{B}\cos(\omega_\mathrm{r}t) + U_0}{l} = m_0\ddot{U}_0, \tag{1}$$

where F_T and F_B are the forces in the connecting bars. Eq. (1) involves the observable fields F and U_0, as well as the internal fields F_T, F_B, r_T, and r_B. Next, efforts are made to eliminate the internal fields, as described in detail in Appendix A. Eventually, under the assumption that the displacement U_0 is infinitely small in magnitude compared to r_T and r_B, the equilibrium Eq. (1) can be expressed via F and U_0 only, given by

$$F = \left[m_0 + 2m_1\cos^2(\omega_\mathrm{r}t)\right]\ddot{U}_0 - 4m_1\dot{U}_0\omega_\mathrm{r}sin(\omega_\mathrm{r}t)\cos(\omega_\mathrm{r}t). \tag{2}$$

It is interesting to find that this formula can be rearranged in accordance with the form of Newton's equation

$$F = \mathrm{d}P_\mathrm{t}/\mathrm{d}t,\ P_\mathrm{t} = m_\mathrm{eff}(t)\dot{U}_0, \tag{3}$$

where P_t denotes the system momentum responded to the force F, and the effective mass $m_\mathrm{eff}(t)$ is given by

$$m_\mathrm{eff}(t) = m_0 + 2m_1\cos^2(\omega_\mathrm{r}t). \tag{4}$$

The above result means that the three-body dynamic system is equivalent to a single body, whose inertial mass $m_\mathrm{eff}(t)$ varies

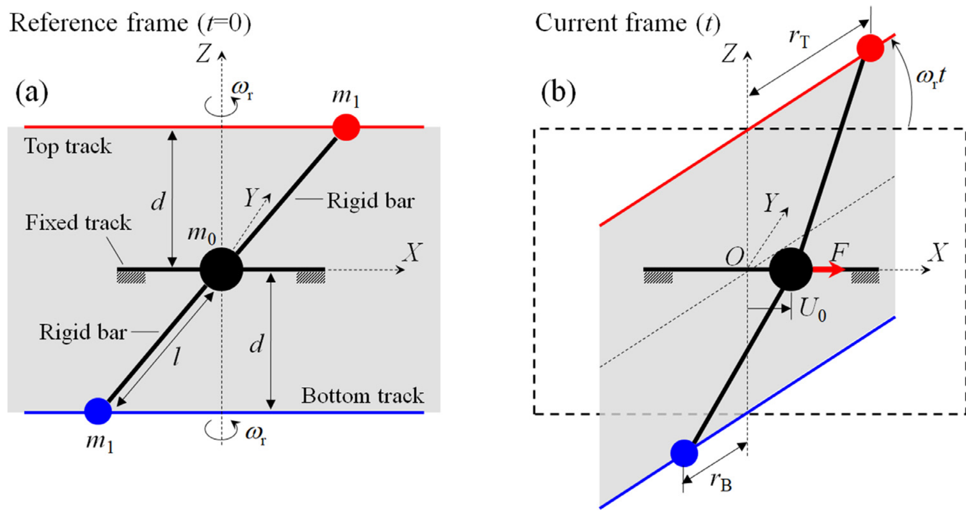

Fig. 1. Schematic diagram of the proposed metamaterial element that exhibits time-varying inertial mass. The element consists of a rigid body of mass m_0 and two additional bodies of mass m_1, interconnected by rigid and massless bars of length l. The m_0-body is constrained to slide on a motionless track, while the sliding tracks on which the m_1-bodies reside rotate at a constant angular velocity ω_r. At an initial time (a), the m_0-body is located at the coordinate origin and the rotating track is directed parallel to the motionless one. After an arbitrary instant t (b), the top and bottom tracks have been rotated with an angle of $\omega_r t$, and the m_0-body may have an offset U_0 to the origin when subject to an external force F.

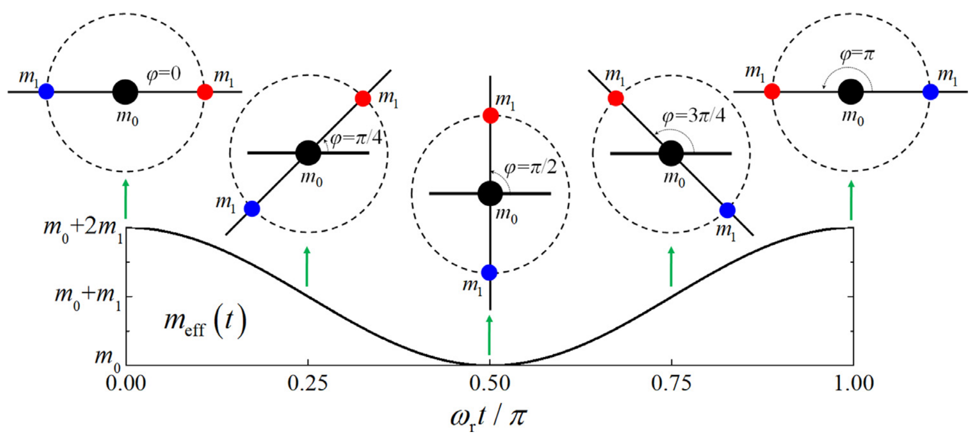

Fig. 2. Effective inertial mass $m_{\text{eff}}(t)$ of the three-body “dynamic” element plotted against the phase angle $\phi = \omega_r t$ in one time period of modulation. Sketched above the curve is the schematic top view of the three-body structure in five specific phases $\varphi = 0, \pi/4, \pi/2, 3\pi/4$, and π.

periodically depending on time in order to take into account the orbiting effect of the m_1-body. The effective mass Eq. (4) can be also written as

$$m_{\text{eff}}(t) = M_0 + M_m \cos(\omega_m t), \tag{5}$$

which is the summation of a constant mass $M_0 = (m_0 + m_1)$ and a periodic modulation of magnitude $M_m = m_1$. The modulation amplitude is $\alpha_m = M_m/M_0$ by definition. ω_m is the modulation frequency, which is twice the rotation frequency, i.e., $\omega_m = 2\omega_r$.

Note that in Section 2.1, it has been assumed that the x axis coincides with the X axis. If the two axes are not parallel, forming an angle φ_0 instead, effective time-varying inertial mass can still be defined, but Eq. (5) need be modified by adding a phase shift $\theta_0 = 2\varphi_0$ to the time-varying part, and written ultimately as

$$m_{\text{eff}}(t) = M_0[1 + \alpha_m \cos(\omega_m t + \theta_0)]. \tag{6}$$

This equation acts as the general formula of time-varying inertial mass of the three-body model.

2.3. Physical explanation of time-dependent inertial mass

Fig. 2 shows effective inertial mass $m_{\text{eff}}(t)$ plotted against the phase angle $\varphi = \omega_r t$ in one time period of modulation. Consider five different phases $\varphi = 0, \pi/4, \pi/2, 3\pi/4$, and π. The schematic top view of the three-body system illustrates the respective model geometry. The result states that the temporal change of effective mass is linked to the change of the model geometry at various instants. To get a deeper physical insight into the time-dependent mass, we consider a time-invariant three-body model, wherein the top and bottom tracks are "frozen" at those five instants. In the case wherein the tracks are parallel to each other ($\varphi = 0$), all bodies would move in exactly the same manner. Hence, the total momentum is $P_t = (m_0 + 2m_1)\dot{U}_0$, which results in the effective mass $m_{\text{eff}} = m_0 + 2m_1$. This is also the case in which the translational momentum of the system reaches the maximum among all temporal phases. The other limiting case with the minimum system momentum arrives when the two tracks are oriented perpendicularly ($\varphi = \pi/2$). Here, the contribution of orbiting bodies vanishes and the total momentum is $P_t = m_0\dot{U}_0$, leading to the effective mass $m_{\text{eff}} = m_0$. In a general case of an

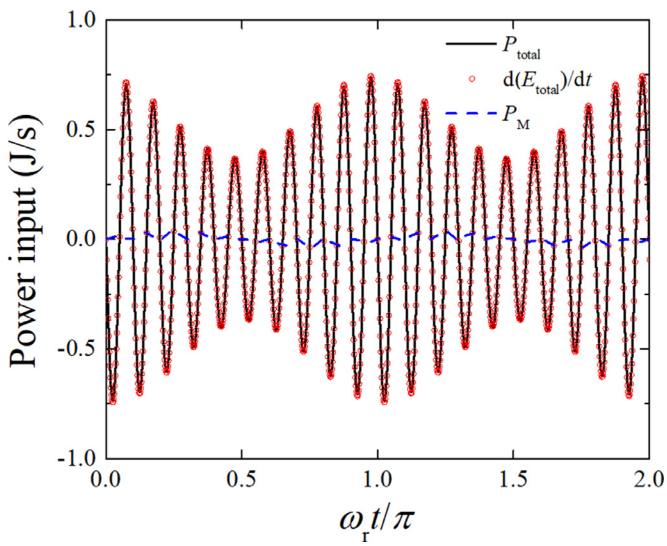

Fig. 3. The instantaneous power input $P_{total} = P_F + P_M$ and P_M in time domain, as well as the time rate of change of the total kinetic energy $d(E_{total})/dt$.

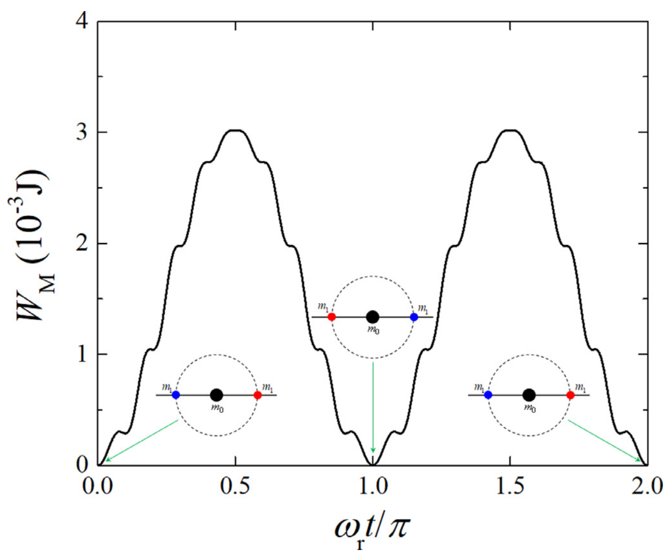

Fig. 4. The work done in time domain to maintain the constant rotation of the top and bottom tracks.

arbitrary angle φ, the X-component velocity of m_1-bodies are $\cos^2(\varphi)\dot{U}_0$, which can be readily derived considering their geometric relations. The total translational momentum is then obtained as $P_t = [m_0 + 2m_1\cos^2(\varphi)]\dot{U}_0$, which would lead to the same effective mass as in Eq. (4). When $\varphi = \pi/4$ or $\varphi = 3\pi/4$, we get $m_{eff} = m_0 + m_1$. Now, it has become quite clear that effective inertial mass of the dynamic system at some instant is the same as that of the non-dynamic system with the corresponding model geometry at that instant. Effective inertial mass would change continually and periodically over time if the top and bottom tracks are "unfrozen" and rotated. One result of the rotation of the tracks is the generation of Coriolis force and centripetal force acting on the m_1-body. However, the Coriolis force produces no effect on the translational momentum, as explained in Appendix A. In addition, the influence of the centripetal force exerted from one body m_1 has been entirely canceled out by the opposite forces from the other body m_1 on the other rotating track. This explains why two oppositely arranged orbiting bodies are considered in the model.

Next, let us analyze the energy that needs to be input to the three-body system to achieve the time-varying mass. The energy input to the system comprises two parts. The first part of the energy refers to the case without any external loadings. It is the work done to the rotating tracks such that the m_1-body initially at rest acquires the kinetic energy to move circularly. The second part of the energy input is for maintaining the constant angular frequency ω_r of the rotating tracks, when the m_0-body is subject to the external excitation. To quantify this part of the energy, consider that the main body undergoes the harmonic oscillation over time with the displacement

$$U_0(t) = \hat{U}_0 \sin(\omega t), \tag{7}$$

where $\hat{U}_0$ is the amplitude and ω is the oscillation frequency. Then, the force $F(t)$ applied to the main body and the moment of force applied to the top and bottom tracks for maintaining the constant rotation can be determined, as given in Appendix B. Let the rate of work done by $F(t)$ and the moment of force be denoted as P_F and P_M, respectively. As an example, we choose the following parameters: $d = 12$ cm, $l = 20$ cm, $m_0 = 30$ g, $m_1 = 15$ g, $\omega_r = 2\pi$ rad/s, and $\omega = 20\pi$ rad/s. Fig. 3 shows the total instantaneous power input, i.e., $P_{total} = P_F + P_M$, as well as the time rate of change of the total kinetic energy $d(E_{total})/dt$. Excellent agreement between P_{total} and $d(E_{total})/dt$ can be found, which is indicative of energy conservation. The power input P_M needed to maintain the constant rotation of the top and bottom tracks is also plotted, which represents only a small portion of the total energy. We further compute the net work done on the rotating tracks by integrating the power input $W_M = \int_0^t P_M dt$, as presented in Fig. 4. The result shows that the energy pumps in and is later taken out from the system. Notice that there is no net work done on the rotating tracks, i.e., $W_M = 0$, during half of the rotation period. This means that it costs no energy in total to maintain the constant rotation of the tracks.

3. Non-reciprocal wave phenomena induced by spatiotemporal modulation of inertial mass

By proposing the three-body dynamic model, we have demonstrated how to modulate the inertial mass in time. In this section, we present the design of the lattice metamaterial whose inertial mass is tailored to be periodically changed in both space and time. The Bloch-based method will be adopted for the computation of dispersion diagrams of periodic metamaterials, allowing us to identify the non-reciprocal directional wave behavior, which occurs when the wave-like modulation is imposed. The effect of modulating parameters on unidirectional bandgaps will be detailed by numerical examples.

3.1. Configuration of space-time lattice metamaterials

The space-time lattice metamaterial is assembled by infinite three-body elements, which are arranged in a straight line, and primary bodies in adjacent cells are separated with the distance a, and connected by springs of the stiffness K, as schematically shown in Fig. 5. Every R elements are grouped into a super cell, acting as the periodical unit of the modulated metamaterial. According to the effective-mass representation, each cell structure behaves as a rigid body with the time-varying inertial mass. Based on the formula (6), we then denote the inertial mass $m^{(r)}(t)$ of the rth element in one super cell as

$$m^{(r)}(t) = M_0\left[1 + \alpha_m \cos\left(\omega_m t + \theta_0^{(r)}\right)\right], \quad r = 1, 2, \ldots, R, \tag{8}$$

where the spatial modulation can be acquired due to the different initial phase $\theta_0^{(r)}$. Let the space and time period of modulation be denoted by $\lambda_m = Ra$ and $T_m = 2\pi/\omega_m$, respectively. They have constituted the "pump" wave with the velocity $v_m = \lambda_m/T_m$, which is the core factor inducing the non-reciprocal wave phenomena (Nassar et al., 2017a; Vila et al., 2017). In the following,

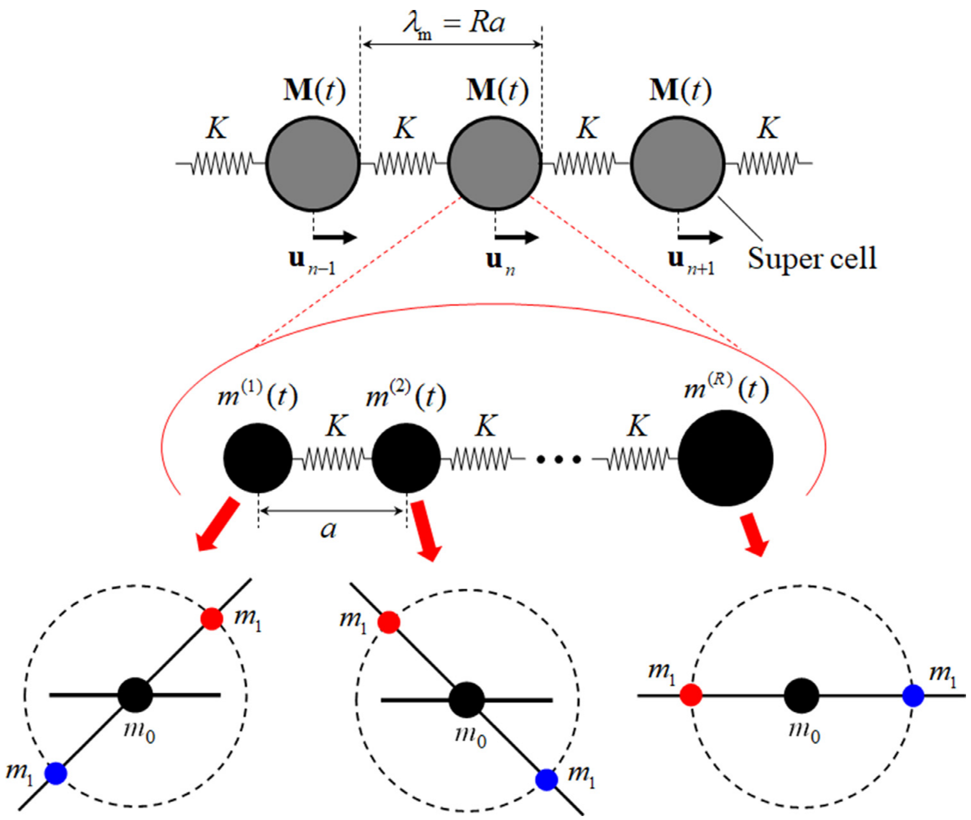

Fig. 5. Schematic of the space-time lattice metamaterial composed of the time-varying mass and springs of constant stiffness K. Every R elements are grouped as a super cell, which is repeated in space with the periodicity Ra. Different initial biasing angles, assigned for different elements in the super cell, provide the spatial modulation of inertial mass, which together with the inherent time-varying property, constitute the space-time modulation that would lead to the non-reciprocal propagation of lattice waves.

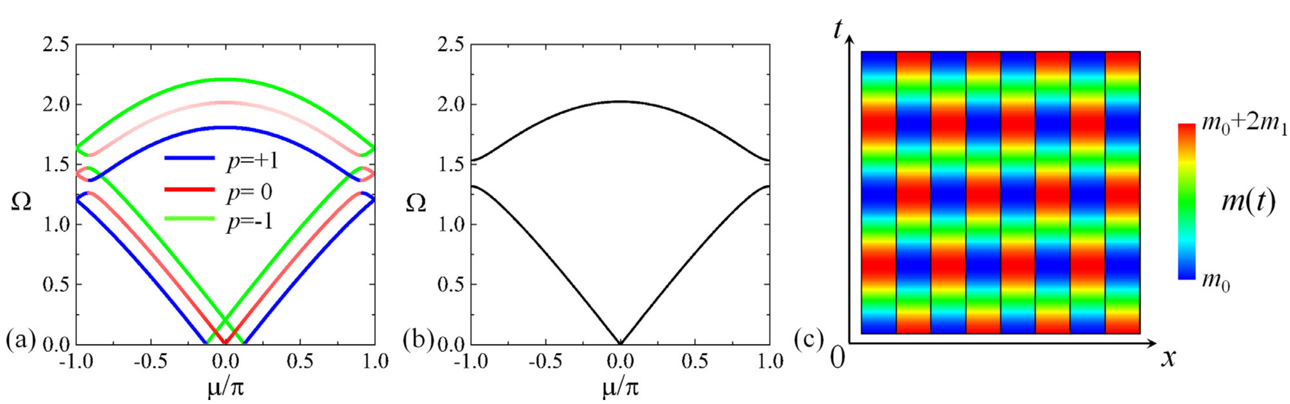

Fig. 6. Dispersion diagrams of the lattice system comprising two elements in each super cell with (a) and without (b) the temporal modulation. (c) The spatiotemporal field pattern of the modulated lattice. The modulating parameters $\alpha_{\mathrm{m}} = 0.15$ and $\omega_{\mathrm{m}} = 0.2\omega_0$, and the initial phases $\theta_0^{(1)} = \pi$ and $\theta_0^{(2)} = 0$ are used.

we will first introduce the method for the dispersion estimation of the space-time lattice metamaterials, and then analyze the non-reciprocal wave phenomena by numerical examples.

The equation of motion generalized for the nth supercell can be grouped as

$$\dot{\mathbf{M}}(t)\dot{\mathbf{u}}_n + \mathbf{M}(t)\ddot{\mathbf{u}}_n + \mathbf{K}^{(l)}\mathbf{u}_{n-1} + \mathbf{K}\mathbf{u}_n + \mathbf{K}^{(r)}\mathbf{u}_{n+1} = 0, \tag{9}$$

where $\mathbf{u}_n = [u_n^{(1)}, u_n^{(2)}, \ldots, u_n^{(R)}]^T$ is the set of displacements of primary bodies. $\mathbf{M}(t)$ is the corresponding mass matrix, and $\mathbf{K}$, $\mathbf{K}^{(l)}$, and $\mathbf{K}^{(r)}$ are stiffness matrices associated to the supercell itself and its relationship to left and right neighboring cells, respectively. The dispersion relation of the modulated superlattice can be estimated by pursuing a plane wave solution

$$\mathbf{u}_n(t) = \mathbf{a}(t)e^{i(\omega t - nk\lambda_{\mathrm{m}})}, \tag{10}$$

where k is the wavenumber of the Bloch wave and $\mathbf{a}(t)$ is the modulated amplitude, which is a periodic function of time, i.e., satisfying $\mathbf{a}(t) = \mathbf{a}(t + T_{\mathrm{m}})$. The function $\mathbf{a}(t)$ can be expanded as the Fourier series in the following form

$$\mathbf{a}(t) = \sum_{p=-\infty}^{\infty} \mathbf{a}_p e^{ip\omega_{\mathrm{m}} t}, \tag{11}$$

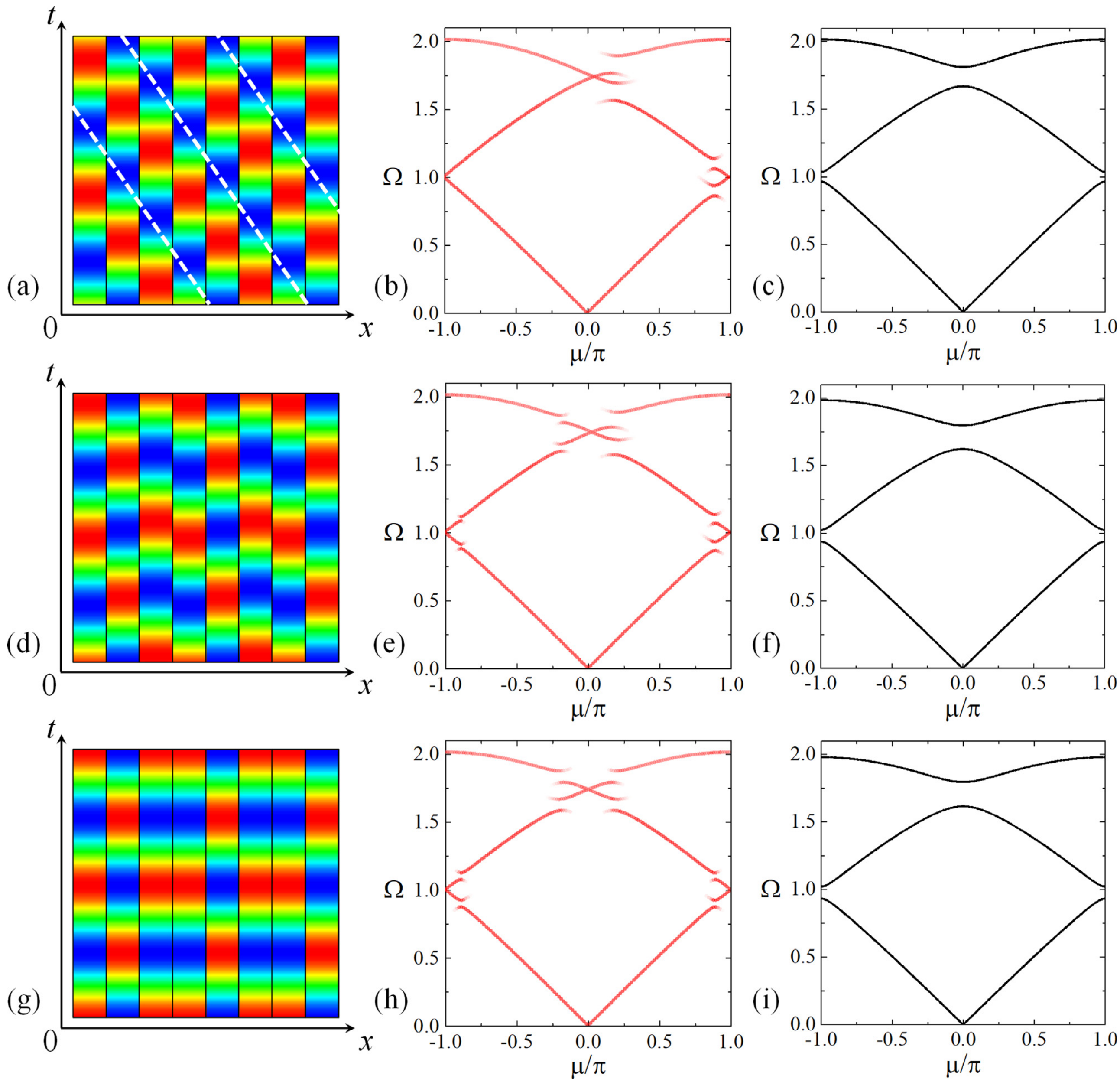

Fig. 7. The spatiotemporal field pattern and fundamental dispersion branch of the modulated metamaterial (with $R=3$) for three different sets of initial phases: (a, b) $\theta_0^{(1)}=\pi/3$, $\theta_0^{(2)}=\pi$, and $\theta_0^{(3)}=5\pi/3$; (d, e) $\theta_0^{(1)}=\pi/8$, $\theta_0^{(2)}=\pi$, and $\theta_0^{(3)}=15\pi/8$; (g, h) $\theta_0^{(1)}=0$, $\theta_0^{(2)}=\pi$, and $\theta_0^{(3)}=0$. (c, f, i) Dispersion curves of the corresponding non-modulated lattice metamaterial.

where $\mathbf{a}_p$ is the coefficient of order p. It follows from Eq. (10) that

$$\mathbf{u}_{n-1}(t)=e^{i\mu}\mathbf{u}_n(t),\ \mathbf{u}_{n+1}(t)=e^{-i\mu}\mathbf{u}_n(t), \tag{12}$$

where the normalized wavenumber $\mu=k\lambda_m$ has been defined. Substituting Eq. (12) into (9), and then following the procedure of the Nassar and Vila's studies (Nassar et al., 2017a; Vila et al., 2017), the quadratic eigenvalue equation can be obtained, the detailed derivation of which is shown in Appendix C. The dispersion relations of the spatiotemporal superlattice can be attained by solving the eigenvalue problem for angular frequency ω in the given wavenumber μ.

3.2. Non-reciprocal wave phenomena in modulated metamaterials

It is evident that the monatomic lattice ($R=1$) is a trivial model of the non-reciprocity as the mass distribution in space is always homogeneous. We begin our analysis with the diatomic model ($R=2$), in which each super cell contains two “dynamic” elements. Consider the modulating parameters $\alpha_{\mathrm{m}}=0.15$ and $\omega_{\mathrm{m}}=0.2\omega_0$ for all elements and choose the set of initial phases as $\theta_0^{(1)}=\pi$ and $\theta_0^{(2)}=0$. Fig. 6(a) shows the band diagrams plotted by the wave number μ as a function of the normalized frequency $\Omega=\omega/\omega_0$, where $\omega_0=\sqrt{K/M_0}$. The truncation order $P=1$ is chosen in the computation. The filtering method proposed by Vila Vila et al., 2017) has been adopted to distinguish the fundamental mode ($p=0$) and the first-order branches ($p=-1,+1$), as marked in the band diagram. The procedure to retrieve the fundamental branch is exemplified here. By substituting (11) into (10), we get the displacement field $\mathbf{u}_n(t)=\sum_{p=-\infty}^{\infty}\mathbf{a}_p e^{i[(\omega+p\omega_{\mathrm{m}})t-n\mu]}$ for the nth supercell. The fundamental branch has an amplitude that is related to the leading term of $p=0$. Hence, it can be identified by weighting the magnitude of the zeroth-order eigenvector $\mathbf{a}_0$ for each

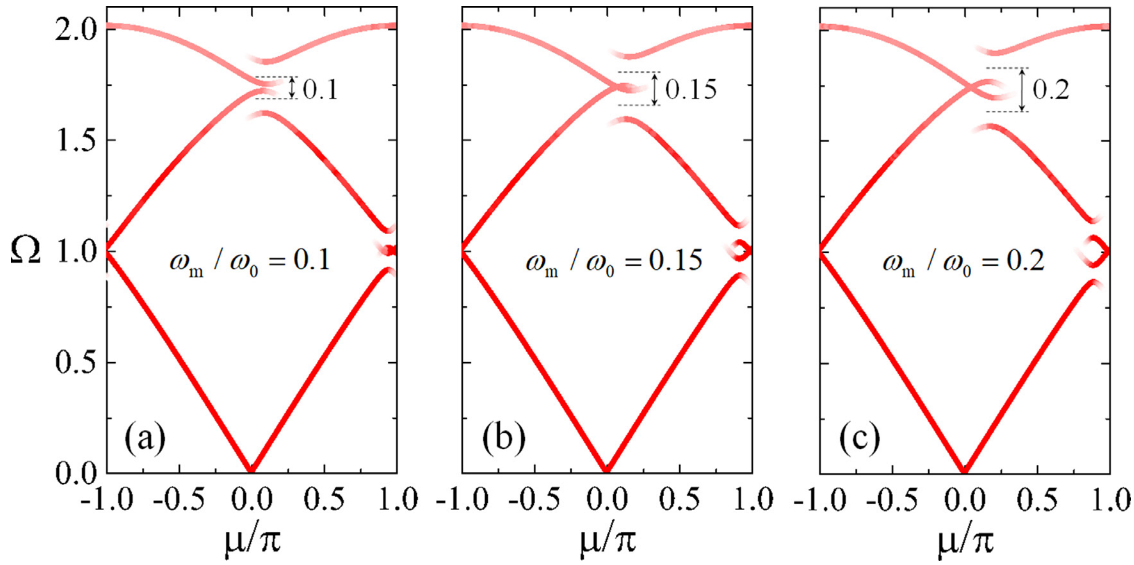

Fig. 8. The fundamental dispersion branch of the modulated metamaterial (with $R=3$) having system parameters $\theta_0^{(1)} = \pi/3$, $\theta_0^{(2)} = \pi$, $\theta_0^{(3)} = 5\pi/3$, $\alpha_m = 0.15$ and three different modulating frequencies $\omega_m/\omega_0 = 0.1$ (a), 0.15 (b), and 0.2 (c).

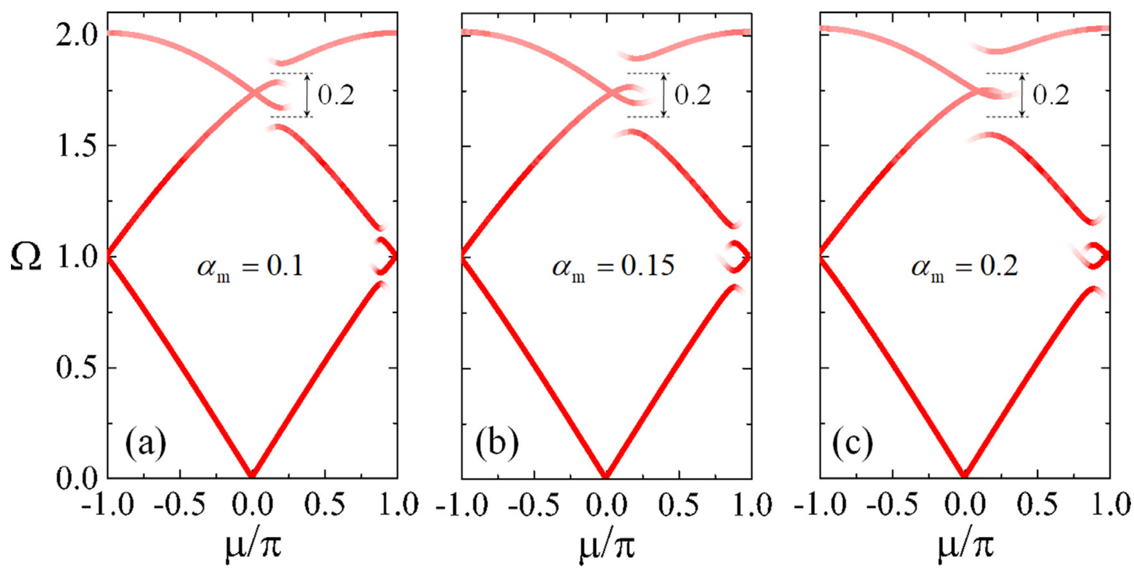

Fig. 9. The fundamental dispersion branch of the modulated metamaterial (with $R=3$) having system parameters $\theta_0^{(1)} = \pi/3$, $\theta_0^{(2)} = \pi$, $\theta_0^{(3)} = 5\pi/3$, $\omega_m/\omega_0 = 0.2$ and three different modulating amplitudes $\alpha_m = 0.1$ (a), 0.15 (b), and 0.2 (c).

branch, and applying a filtering value to avoid plotting high-order branches. Other branches can be likewise retrieved using this filtering method. Below, we focus mainly on the fundamental mode as it usually stores a large portion of the system energy. As a comparison, Fig. 6(b) shows the band structure of the non-modulated lattice ($\omega_m = 0$), in which symmetric band gaps are opened due to the spatial periodicity of inertial mass. When the time modulation is added (Fig. 6(a)), they are split due to the time-driven mode interaction. The upper gap results from the interaction of the 0th order and the -1th order modes, while the lower one is the result of the mode interaction of the 0th and $+1$th orders (Cassedy and Oliner, 1963). Nevertheless, the band structures are still symmetric with respect to the forward and backward directions. To gain further insights, we illustrate the spatiotemporal field pattern of inertial mass in Fig. 6(c). We can then understand symmetric dispersion branches from the overall standing-wave pattern, which is of the mirror symmetry if folded along the time axis. In other words, this kind of pattern impacts the forward and backward waves equally as the standing wave is the superposition of forward and backward travelling waves of equal amplitude. This example illustrates that more band gaps can be produced in the space-time diatomic lattice, yet they are still symmetric since the system supports only the standing-wave modulation pattern.

We continue to analyze wave dispersions of the lattice system with $R=3$. Consider the modulating parameters $\alpha_m = 0.15$, and $\omega_m = 0.2\omega_0$, and let the initial phases be $\theta_0^{(1)} = \pi/3$, $\theta_0^{(2)} = \pi$ and $\theta_0^{(3)} = 5\pi/3$. Fig. 7(a)–(c) show the space-time field patterns of mass and dispersion diagrams of the fundamental branch in both the presence and absence of time modulation. Note that these initial phases have been chosen specifically so that the phase difference between any two adjacent elements remains the same, namely $\Delta\theta_0 = 2\pi/3$. Consequently, the field pattern shows the profile of the backward traveling wave, which breaks the spatial inversion symmetry, as shown in Fig. 7(a). This has led to the bandgaps that can only be observed in the forward direction due to the time-driven mode interaction (Fig. 7(b)). It means that only the backward wave propagation is allowed at the gap frequencies. Fig. 7(d) shows the field pattern for a different set of initial phases $\theta_0^{(1)} = \pi/8$, $\theta_0^{(2)} = \pi$, and $\theta_0^{(3)} = 15\pi/8$, which are designed in such a way that the backward modulation wave is superimposed by a weak modulation of the forward one. Accordingly, in addition to the gap opened in the positive wave-vector space, a narrower gap is created in the negative one (Fig. 7(e)). In another case where any two initial phases are chosen as the same, e.g., $\theta_0^{(1)} = \theta_0^{(3)} = 0$, and $\theta_0^{(2)} = \pi$, the standing-wave field pattern will be recovered (Fig. 7(g)), resulting in symmetric dispersions as shown in Fig. 7(h). The observed reciprocal wave phenomenon is similar to what happens in the modulated diatomic lattice. In the above three cases, the dispersion diagrams in the absence of time modulation look very similar, as evidenced in Fig. 7(c, f, and i). This highlights again that the initial phase distribution, which determines the space-time field pattern of mass, is a critical parameter for asymmetric wave manipulation.

We now evaluate the effect of modulating frequency and amplitude, i.e., ω_m and α_m, on the wave non-reciprocity by choosing the initial phases used in Fig. 7(a), which would result in purely unidirectional bandgaps. Fig. 8(a)–(c) show the fundamental branches of the modulated crystal with $\alpha_m = 0.15$, and three different modulating frequencies $\omega_m/\omega_0 = 0.1$, 0.15, and 0.2, respectively. It can be found that asymmetric gaps are opened as long as $\omega_m \neq 0$. Moreover, as a result of the time modulation, the central-frequency difference between the upper and lower gaps is exactly equal to ω_m/ω_0. The analogous phenomenon has also been observed previously in a space-time lattice composed of constant mass and time-driven springs (Vila et al., 2017). These results indicate that the modulation frequency ω_m plays a crucial role in tuning the asymmetric gap frequency. Notice that the direction of asymmetric bandgaps can be reversed if one changes the sign of ω_m. To examine the effect of α_m, we consider $\omega_m/\omega_0 = 0.2$ and three different modulation amplitudes $\alpha_m = 0.1$, 0.15, and 0.2. The resulting fundamental branches are shown in Fig. 9. It is observed that increasing α_m has an obvious effect on widening the bandwidth of the asymmetric bandgap. It is also worth mentioning that the central-frequency difference between the gaps remains invariant because $\omega_m/\omega_0 = 0.2$ is unchanged among those three cases.

Based on the above analysis, we have confirmed that non-reciprocal wave propagation can be gained by the spatiotemporal modulation of mass. It is found that the initial phase $\theta_0^{(r)}$ ($r = 1, 2, \ldots, R$), modulating frequency ω_m, and amplitude α_m are three fundamental parameters controlling the opening of asymmetric bandgap, the relevant frequency position, and the bandwidth, respectively; in the three-body "dynamic" model, these three controlling parameters correspond to the initial position of orbiting bodies, the angular frequency of rotation, and the weight ratio between the orbiting and primary bodies, respectively.

4. Conclusion

The metamaterial concept, which has been employed in the past to achieve time-invariant material properties, e.g., negative inertial mass and/or negative modules, is extended here to include the time-dependent inertial mass. The design for "dynamic" metamaterials follows the principle that the microstructure need not be at rest even without any external loadings. The proposed metamaterial element is a three-body structure, wherein the primary body is seen as the observable DOF, while the other two bodies that move along a circular orbit are designed as the hidden DOFs. Rigorous theoretical analyses have shown that the translational momentum contributed by the moving bodies varies periodically depending on their temporal phases. In the case of small oscillation, an effective inertial mass that retains the meaning from Newton's second law of motion can be defined, which is found to be a periodic function of time.

Based on the proposed "dynamic" cell, we have constructed an infinite space-time lattice metamaterial by linking the time-varying mass with springs of constant stiffness. The Bloch-based method was developed for the estimation of dispersion diagrams of the modulated metamaterial. It is found that the travelling-wave field pattern of mass is required for the opening of purely unidirectional bandgaps. The modulating frequency and amplitude of time-varying inertial mass determine the frequency position and bandwidth of non-reciprocal wave phenomena, respectively. They are correlated directly to the angular frequency of rotation and the weight ratio between orbiting and primary bodies in the three-body microstructure. The non-reciprocal wave behavior realized by the spatiotemporal modulation of mass is expected to bring new technological concepts with broad engineering applications in wave and vibration control.

Acknowledgements

This work was supported by the National Natural Science Foundation of China [grant numbers 11872111, 11622215, 11521062, and 11572039] and 111 project [grant number B16003].

Competing interests statement

The authors declare no competing interests.

Appendix A. Dynamic analysis of the three-body system

The equilibrium equation of the m_0-body is written as

$$F - F_T\cos(\varphi_T) - F_B\cos(\varphi_B) = m_0\ddot{U}_0, \tag{A.1}$$

where F_T and F_B are the forces in the top and bottom connecting bars, respectively. φ_T ($= \angle DAC$) and φ_B ($= \angle JAH$) are the included angles between connecting bars and the X axis, as shown in Fig. A.1, which follow the geometric relations

$$\cos\varphi_T = \cos\angle DAB \cdot \cos\angle BAC, \tag{A.2}$$

$$\cos\varphi_B = \cos\angle JAI \cdot \cos\angle IAH. \tag{A.3}$$

The auxiliary angles appearing on the right-hand side of above equations can be computed by

$$\cos\angle DAB = \frac{\sqrt{l^2 - d^2}}{l}, \tag{A.4}$$

$$\cos\angle BAC = \frac{-U_0 + r_T\cos(\omega_r t)}{\sqrt{l^2 - d^2}}, \tag{A.5}$$

$$\cos\angle JAI = \frac{\sqrt{l^2 - d^2}}{l}, \tag{A.6}$$

$$\cos\angle IAH = \frac{U_0 + r_B\cos(\omega_r t)}{\sqrt{l^2 - d^2}}. \tag{A.7}$$

Substituting Eqs. (A.2)–(A.7) into (A.1), we obtain the equilibrium Eq. (1).

Now analyze the kinematics of the rotating bodies. The absolute velocity $\mathbf{V}_T$ of the top m_1-body is expressed in the moving coordinate system as

$$\mathbf{V}_T = \dot{r}_T\mathbf{e}_x + \omega_r r_T\mathbf{e}_y, \tag{A.8}$$

where the first term denotes its velocity relative to the moving system. The second term describes the convected velocity arising from the relative motion of the moving coordinate system with respect to the fixed one. Remember that vectors $\mathbf{e}_x$ and $\mathbf{e}_y$ are functions

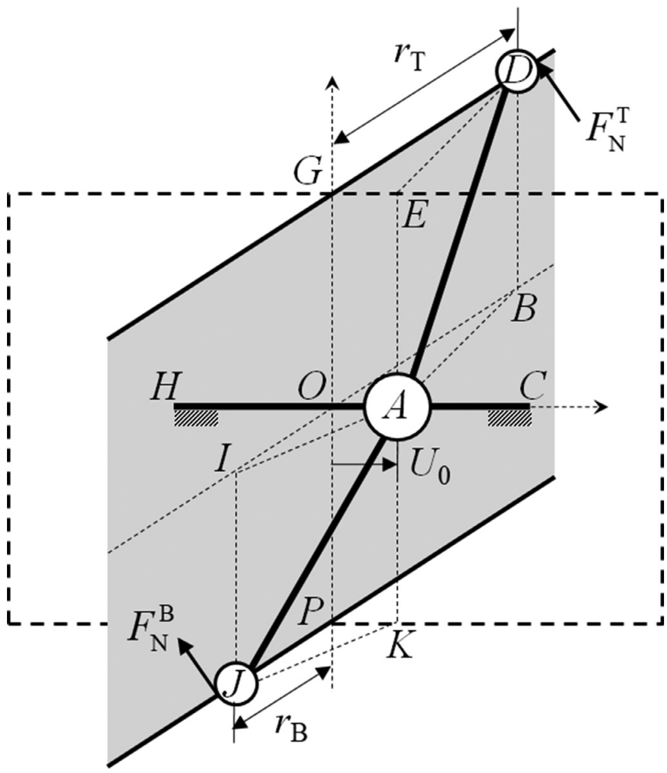

Fig. A.1. A schematic view of geometric configuration of the three-body system.

of time, and are related to the angular frequency ω_r of rotation. By taking the total time derivative of the velocity $\mathbf{V}_T$, we get the absolute acceleration $\mathbf{A}_T$ of the top m_1-body

$$\mathbf{A}_T = \ddot{r}_T\mathbf{e}_x - \omega_r^2 r_T\mathbf{e}_x + 2\omega_r\dot{r}_T\mathbf{e}_y. \tag{A.9}$$

The first two terms denote again the relative and convected accelerations. The third term refers to the Coriolis acceleration, which points toward the y axis. The determination of F_T concerns only the equilibrium equation in the $\mathbf{e}_x$ direction; hence, the Coriolis acceleration force produces no effect. We then have

$$F_T\cos\varphi'_T = m_1\left(\ddot{r}_T - \omega_r^2 r_T\right), \tag{A.10}$$

where $\varphi'_T = \angle GDA$ is the angle between the bar and the top track, and can be calculated by

$$\cos\varphi'_T = \frac{r_T - U_0\cos(\omega_r t)}{l}, \tag{A.11}$$

in which the following geometric equations have been used

$$\cos\varphi'_T = \cos\angle EDA \cdot \cos\angle GDE,$$
$$\cos\angle EDA = \frac{\sqrt{l^2 - d^2}}{l},\ \cos\angle GDE = \frac{r_T - U_0\cos(\omega_r t)}{\sqrt{l^2 - d^2}}.$$

Substitution of Eqs. (A.11) into (A.10) yields the force-displacement relationship pertaining to the top m_1-body

$$F_T = \frac{m_1 l\left(\ddot{r}_T - \omega_r^2 r_T\right)}{r_T - U_0\cos(\omega_r t)}. \tag{A.12}$$

Similarly, we can write the absolute velocity $\mathbf{V}_B$ and acceleration $\mathbf{A}_B$ of the bottom m_1-body as

$$\mathbf{V}_B = -\dot{r}_B\mathbf{e}_x - \omega_r r_B\mathbf{e}_y, \tag{A.13}$$

$$\mathbf{A}_B = -\ddot{r}_B\mathbf{e}_x + \omega_r^2 r_B\mathbf{e}_x - 2\omega_r\dot{r}_B\mathbf{e}_y. \tag{A.14}$$

Its equilibrium equation reads

$$F_B\cos\varphi'_B = m_1\left(-\ddot{r}_B + \omega_r^2 r_B\right), \tag{A.15}$$

where $\varphi'_B = \angle PJA$ can be computed by

$$\cos\varphi'_B = \frac{r_B + U_0\cos(\omega_r t)}{l}, \tag{A.16}$$

which is obtained by using the following relations

$$\cos\varphi'_B = \cos\angle KJA \cdot \cos\angle PJK,$$
$$\cos\angle KJA = \frac{\sqrt{l^2 - d^2}}{l},\ \cos\angle PJK = \frac{r_B + U_0\cos(\omega_r t)}{\sqrt{l^2 - d^2}}.$$

By substituting Eqs. (A.16) into (A.15), we find that

$$F_B = \frac{m_1 l\left(\omega_r^2 r_B - \ddot{r}_B\right)}{r_B + U_0\cos(\omega_r t)}. \tag{A.17}$$

Eliminate F_T and F_B by substituting Eqs. (A.12) and (A.17) into (1), leading to

$$F - m_1\left(\ddot{r}_T - \omega_r^2 r_T\right)\frac{r_T\cos(\omega_r t) - U_0}{r_T - U_0\cos(\omega_r t)}$$
$$+ m_1\left(\ddot{r}_B - \omega_r^2 r_B\right)\frac{r_B\cos(\omega_r t) + U_0}{r_B + U_0\cos(\omega_r t)} = m_0\ddot{U}_0. \tag{A.18}$$

To further eliminate the internal fields r_T and r_B in Eq. (A.18), let us examine the distance between the primary body and the two orbiting bodies. It is easy to find the following geometric equation

$$l^2 = \left[r_T\cos(\omega_r t) - U_0\right]^2 + \left[r_T\sin(\omega_r t)\right]^2 + d^2, \tag{A.19}$$

$$l^2 = \left[r_B\cos(\omega_r t) + U_0\right]^2 + \left[r_B\sin(\omega_r t)\right]^2 + d^2. \tag{A.20}$$

For convenience, the above equations are rearranged as

$$U_0^2 + r_T^2 - 2r_T U_0\cos(\omega_r t) = l^2 - d^2, \tag{A.21}$$

$$U_0^2 + r_B^2 + 2r_B U_0\cos(\omega_r t) = l^2 - d^2. \tag{A.22}$$

Taking the time derivative of Eqs. (A.21) and (A.22) leads to

$$U_0\dot{U}_0 + r_T\dot{r}_T - \left(\dot{r}_T U_0 + r_T\dot{U}_0\right)\cos(\omega_r t) + r_T U_0\omega_r\sin(\omega_r t) = 0, \tag{A.23}$$

$$U_0\dot{U}_0 + r_B\dot{r}_B + \left(\dot{r}_B U_0 + r_B\dot{U}_0\right)\cos(\omega_r t) - r_B U_0\omega_r\sin(\omega_r t) = 0. \tag{A.24}$$

Taking again the time derivative of above two equations, we have

$$\dot{U}_0^2 + U_0\ddot{U}_0 + \dot{r}_T^2 + r_T\ddot{r}_T - \left(\ddot{r}_T U_0 + 2\dot{r}_T\dot{U}_0 + r_T\ddot{U}_0 - r_T U_0\omega_r^2\right)\cos(\omega_r t)$$
$$+ 2\omega_r\left(\dot{r}_T U_0 + r_T\dot{U}_0\right)\sin(\omega_r t) = 0, \tag{A.25}$$

$$\dot{U}_0^2 + U_0\ddot{U}_0 + \dot{r}_B^2 + r_B\ddot{r}_B + \left(\ddot{r}_B U_0 + 2\dot{r}_B\dot{U}_0 + r_B\ddot{U}_0 - r_B U_0\omega_r^2\right)\cos(\omega_r t)$$
$$-2\omega_r\left(\dot{r}_B U_0 + r_B\dot{U}_0\right)\sin(\omega_r t) = 0. \tag{A.26}$$

Assume that the displacement U_0 is infinitely small in magnitude compared to r_T and r_B, i.e., $U_0/r_T, U_0/r_B \ll 1$, which is practically possible if the small-amplitude force F is applied, or if relatively large l and d are chosen. Under this assumption, it can be deduced from Eqs. (A.21) and (A.22) that

$$U_0 \ll r_T \approx r_B. \tag{A.27}$$

However, the result $r_T \approx r_B$ does not imply the equality of the time derivative and double time derivative of r_T and r_B. Simplifying Eqs. (A.23) and (A.24) by use of (A.27) gives rise to

$$\dot{r}_T \approx \dot{U}_0\cos(\omega_r t) - U_0\omega_r\sin(\omega_r t), \tag{A.28}$$

$$\dot{r}_B \approx -\dot{U}_0\cos(\omega_r t) + U_0\omega_r\sin(\omega_r t). \tag{A.29}$$

Likewise, we can simplify Eqs. (A.25) and (A.26) by using (A.27)–(A.29) to find that

$$\ddot{r}_{\mathrm{T}} \approx -2\dot{U}_0\omega_{\mathrm{r}} \sin(\omega_{\mathrm{r}}t) - \left(\dot{U}_0^2/r_{\mathrm{T}}\right)\sin^2(\omega_{\mathrm{r}}t) + \left(\ddot{U}_0 - U_0\omega_{\mathrm{r}}^2\right)\cos(\omega_{\mathrm{r}}t), \tag{A.30}$$

$$\ddot{r}_{\mathrm{B}} \approx 2\dot{U}_0\omega_{\mathrm{r}} \sin(\omega_{\mathrm{r}}t) - \left(\dot{U}_0^2/r_{\mathrm{B}}\right)\sin^2(\omega_{\mathrm{r}}t) - \left(\ddot{U}_0 - U_0\omega_{\mathrm{r}}^2\right)\cos(\omega_{\mathrm{r}}t). \tag{A.31}$$

By substituting Eqs. (A.30) and (A.31) into (A.18), and considering the condition (A.27), we acquire the final form of the equilibrium equation of the m_0-body, which is expressed in terms of F and U_0 only, as shown by Eq. (2).

Appendix B. Energy analysis of the three-body system

Calculation of the power input $P_{\mathrm{F}}(t)$. Given the displacement $U_0(t)$, the force $F(t)$ applied to the main body can be calculated approximately from Eq. (3), and is given by

$$F(t) = m_{\mathrm{eff}}(t)\ddot{U}_0(t) + \dot{m}_{\mathrm{eff}}(t)\dot{U}_0(t). \tag{B.1}$$

Note that $F(t)$ should be calculated from Eq. (A.18) in the general case. Substitution of the Eq. (7) into (B.1) results in

$$F(t) = -m_0\omega^2\hat{U}_0 \sin(\omega t) - 2m_1\omega^2\hat{U}_0\cos^2(\omega_{\mathrm{r}}t)\sin(\omega t) - 2m_1\omega_{\mathrm{r}}\omega\hat{U}_0 \sin(2\omega_{\mathrm{r}}t)\cos(\omega t). \tag{B.2}$$

The instantaneous power input $P_{\mathrm{F}}(t)$, i.e., the rate of work done by $F(t)$, can be calculated as

$$P_{\mathrm{F}}(t) = F(t)\mathrm{d}U_0(t)/\mathrm{d}t, \tag{B.3}$$

or explicitly,

$$P_{\mathrm{F}}(t) = -m_0\omega^3\hat{U}_0^2 \sin(2\omega t)/2 - m_1\omega^3\hat{U}_0^2\cos^2(\omega_{\mathrm{r}}t)\sin(2\omega t) - 2m_1\omega_{\mathrm{r}}\omega^2\hat{U}_0^2 \sin(2\omega_{\mathrm{r}}t)\cos^2(\omega t). \tag{B.4}$$

Calculation of the power input $P_{\mathrm{M}}(t)$. The moments of force applied to the top and bottom tracks to maintain the constant rotation are denoted by $M^{\mathrm{T}}(t)$ and $M^{\mathrm{B}}(t)$, respectively, which can be computed according to equilibrium equations

$$M^{\mathrm{T}}(t) + F_{\mathrm{N}}^{\mathrm{T}}(t)r_{\mathrm{T}} = 0, \tag{B.5}$$

$$M^{\mathrm{B}}(t) - F_{\mathrm{N}}^{\mathrm{B}}(t)r_{\mathrm{B}} = 0, \tag{B.6}$$

where $F_{\mathrm{N}}^{\mathrm{T}}(t)$ and $F_{\mathrm{N}}^{\mathrm{B}}(t)$ are the inertial forces of the m_1-body acting on the rotating tracks, as shown in Fig. A.1. Consider the equations of motion of the top m_1-body

$$F_{\mathrm{T}}(\cos\angle EDA \cdot \sin\angle GDE) - F_{\mathrm{N}}^{\mathrm{T}} = 2m_1\omega_{\mathrm{r}}\dot{r}_{\mathrm{T}}, \tag{B.7}$$

$$F_{\mathrm{T}}(\cos\angle EDA \cdot \cos\angle GDE) = m_1\left(\ddot{r}_{\mathrm{T}} - \omega_{\mathrm{r}}^2 r_{\mathrm{T}}\right). \tag{B.8}$$

Substitute Eq. (B.8) into (B.7) to obtain the force$F_{\mathrm{N}}^{\mathrm{T}}$, which is given by

$$F_{\mathrm{N}}^{\mathrm{T}} = m_1\left(\ddot{r}_{\mathrm{T}} - \omega_{\mathrm{r}}^2 r_{\mathrm{T}}\right)\frac{U_0\sin(\omega_{\mathrm{r}}t)}{r_{\mathrm{T}} - U_0\cos(\omega_{\mathrm{r}}t)} - 2m_1\omega_{\mathrm{r}}\dot{r}_{\mathrm{T}}. \tag{B.9}$$

Then from Eq. (B.5), one can get the expression of $M^{\mathrm{T}}(t)$

$$M^{\mathrm{T}}(t) = -m_1 r_{\mathrm{T}}\left(\ddot{r}_{\mathrm{T}} - \omega_{\mathrm{r}}^2 r_{\mathrm{T}}\right)\frac{U_0\sin(\omega_{\mathrm{r}}t)}{r_{\mathrm{T}} - U_0\cos(\omega_{\mathrm{r}}t)} + 2m_1\omega_{\mathrm{r}}\dot{r}_{\mathrm{T}}r_{\mathrm{T}}. \tag{B.10}$$

The rate of work done by the moment of force $M^{\mathrm{T}}(t)$ is calculated as

$$P_{\mathrm{M}}^{\mathrm{T}}(t) = \omega_{\mathrm{r}}M^{\mathrm{T}}(t). \tag{B.11}$$

Similarly, the moment of force $M^{\mathrm{B}}(t)$ relevant to the bottom m_1-body can be derived as

$$M^{\mathrm{B}}(t) = -m_1 r_{\mathrm{B}}\left(-\ddot{r}_{\mathrm{B}} + \omega_{\mathrm{r}}^2 r_{\mathrm{B}}\right)\frac{U_0\sin(\omega_{\mathrm{r}}t)}{r_{\mathrm{B}} + U_0\cos(\omega_{\mathrm{r}}t)} + 2m_1\omega_{\mathrm{r}}\dot{r}_{\mathrm{B}}r_{\mathrm{B}}. \tag{B.12}$$

The rate of work done by $M^{\mathrm{B}}(t)$ is calculated as

$$P_{\mathrm{M}}^{\mathrm{B}}(t) = \omega_{\mathrm{r}}M^{\mathrm{B}}(t). \tag{B.13}$$

Finally, the rate of the net work done by the moment of force is

$$P_{\mathrm{M}}(t) = P_{\mathrm{M}}^{\mathrm{T}}(t) + P_{\mathrm{M}}^{\mathrm{B}}(t). \tag{B.14}$$

Calculation of the time rate of change of the total kinetic energy $\mathrm{d}(E_{\mathrm{total}})/\mathrm{d}t$. The kinetic energies of the main body, and the top and bottom m_1-bodies are

$$E_0(t) = \frac{1}{2}m_0\omega^2\hat{U}_0^2\cos^2(\omega t), \tag{B.15}$$

$$E_1^{\mathrm{T}}(t) = \frac{1}{2}m_1\left(\dot{r}_{\mathrm{T}}^2 + \omega_{\mathrm{r}}^2 r_{\mathrm{T}}^2\right), \tag{B.16}$$

$$E_1^{\mathrm{B}}(t) = \frac{1}{2}m_1\left(\dot{r}_{\mathrm{B}}^2 + \omega_{\mathrm{r}}^2 r_{\mathrm{B}}^2\right). \tag{B.17}$$

The time rate of change of these kinetic energies are given by

$$\mathrm{d}(E_0)/\mathrm{d}t = -m_0\omega^3\hat{U}_0^2\cos(\omega t)\sin(\omega t), \tag{B.18}$$

$$\mathrm{d}\left(E_1^{\mathrm{T}}\right)/\mathrm{d}t = m_1\dot{r}_{\mathrm{T}}\left(\ddot{r}_{\mathrm{T}} + \omega_{\mathrm{r}}^2 r_{\mathrm{T}}\right), \tag{B.19}$$

$$\mathrm{d}\left(E_1^{\mathrm{B}}\right)/\mathrm{d}t = m_1\dot{r}_{\mathrm{B}}\left(\ddot{r}_{\mathrm{B}} + \omega_{\mathrm{r}}^2 r_{\mathrm{B}}\right), \tag{B.20}$$

where r_{T}, r_{B}, and their time derivatives can be computed from Eqs. (A.19), (A.20), and (A.23)–(A.26). Finally, the time rate of change of the total kinetic energy is calculated as

$$\mathrm{d}(E_{\mathrm{total}})/\mathrm{d}t = \mathrm{d}(E_0)/\mathrm{d}t + \left(E_1^{\mathrm{T}}\right)/\mathrm{d}t + \left(E_1^{\mathrm{B}}\right)/\mathrm{d}t. \tag{B.21}$$

Appendix C. Method for dispersion estimation of modulated metamaterials

Substitution of the Eq. (12) into (9) results in

$$\dot{\mathbf{M}}(t)\dot{\mathbf{u}}_n(t) + \mathbf{M}(t)\ddot{\mathbf{u}}_n(t) + \mathbf{K}(\mu)\mathbf{u}_n(t) = 0 \tag{C.1}$$

with

$$\mathbf{K}(\mu) = \mathbf{K}^{(l)}e^{i\mu} + \mathbf{K} + \mathbf{K}^{(r)}e^{-i\mu}. \tag{C.2}$$

Since the mass matrices $\mathbf{M}(t)$ are periodic functions of time, i.e., $\mathbf{M}(t) = \mathbf{M}(t + T_m)$, they can be also expressed as the Fourier series

$$\mathbf{M}(t) = \sum_{q=-\infty}^{\infty}\mathbf{M}_q e^{iq\omega_{\mathrm{m}}t}. \tag{C.3}$$

Combining Eqs. (11) and (C.3), we can express the first two terms of Eq. (C.1) as

$$\begin{aligned}\dot{\mathbf{M}}(t)\dot{\mathbf{u}}_n(t) + \mathbf{M}(t)\ddot{\mathbf{u}}_n(t) = &\left[\sum_{q=-\infty}^{\infty}(iq\omega_{\mathrm{m}})\mathbf{M}_q e^{iq\omega_{\mathrm{m}}t}\right]\\ &\sum_{p=-\infty}^{\infty} i(\omega + p\omega_{\mathrm{m}})\mathbf{a}_p e^{i[-n\mu + (\omega + p\omega_{\mathrm{m}})t]}\\ &-\left(\sum_{q=-\infty}^{\infty}\mathbf{M}_q e^{iq\omega_{\mathrm{m}}t}\right)\\ &\sum_{p=-\infty}^{\infty}(\omega + p\omega_{\mathrm{m}})^2\mathbf{a}_p e^{i[-n\mu + (\omega + p\omega_{\mathrm{m}})t]}\end{aligned} \tag{C.4}$$

Substitution of (C.4) into (C.1) gives rise to

$$\sum_{p=-\infty}^{\infty} \mathbf{M}'_p e^{i[-n\mu+(\omega+p\omega_\mathrm{m})t]} + \mathbf{K}(\mu) \sum_{p=-\infty}^{\infty} \mathbf{a}_p e^{i[-n\mu+(\omega+p\omega_\mathrm{m})t]} = 0, \tag{C.5}$$

where the frequency-dependent matrix $\mathbf{M}'_p(\omega)$ has been introduced, given by

$$\mathbf{M}'_p(\omega) = -\sum_{q=-\infty}^{\infty} (\omega + p\omega_\mathrm{m})[\omega + (p-q)\omega_\mathrm{m}]\mathbf{M}_q \mathbf{a}_{p-q}. \tag{C.6}$$

Now performing the harmonic balance in Eq. (C.5), we get that

$$-\sum_{q=-\infty}^{\infty} (\omega + p\omega_\mathrm{m})[\omega + (p-q)\omega_\mathrm{m}]\mathbf{M}_q \mathbf{a}_{p-q} + \mathbf{K}(\mu)\mathbf{a}_p = 0, \quad p \in (-\infty, +\infty). \tag{C.7}$$

In dispersion calculations, the truncation order P needs to be set for the running number p, such that $\mathbf{a}_p = 0$ for $|p| > P$ (Vila et al., 2017). This means that $p \in [-P, +P]$ and $q \in [p-P, p+P]$. Consequently, the expression (C.7) involves $R \times (2P+1)$ equations in total, and can be cast in the form of a quadratic eigenvalue equation

$$\left[\omega^2 \mathbf{L}_2(\mu) + \omega \mathbf{L}_1(\mu) + \mathbf{L}_0(\mu)\right]\mathbf{a}_\mathrm{total} = 0, \tag{C.8}$$

where $\mathbf{a}_\mathrm{total}$ contains all unknowns. $\mathbf{L}_0(\mu)$, $\mathbf{L}_1(\mu)$, and $\mathbf{L}_2(\mu)$ are known matrices relevant to the wavenumber μ only. The dispersion relations of the modulated superlattice can be attained by solving the eigenvalue problem in Eq. (C.8) for angular frequency ω in the given wavenumber μ.

For example, if $R=3$, the mass matrices $\mathbf{M}(t)$ in (C.1) are written as

$$\mathbf{M}(t) = \begin{bmatrix} m^{(1)}(t) & 0 & 0 \\ 0 & m^{(2)}(t) & 0 \\ 0 & 0 & m^{(3)}(t) \end{bmatrix}. \tag{C.9}$$

Fourier coefficients $\mathbf{M}_q$ appearing in Eq. (C.7) are obtained by integrating $\mathbf{M}(t)$ over one time period T_m of modulation, given by

$$\mathbf{M}_q = \frac{1}{T_\mathrm{m}} \int_{-T_\mathrm{m}/2}^{T_\mathrm{m}/2} \mathbf{M}(t) e^{-iq\omega_\mathrm{m}t} dt. \tag{C.10}$$

Suppose that the truncation order $P=1$ is chosen. According to the Formula (8), the mass matrices $\mathbf{M}_{-1}$, $\mathbf{M}_0$, and $\mathbf{M}_{+1}$ are derived as

$$\mathbf{M}_{-1} = \frac{M_0\alpha_\mathrm{m}}{2} \mathrm{diag}\left[e^{-i\theta_0^{(1)}}, e^{-i\theta_0^{(2)}}, e^{-i\theta_0^{(3)}}\right], \tag{C.11}$$

$$\mathbf{M}_0 = M_0 \mathrm{diag}[1, 1, 1], \tag{C.12}$$

$$\mathbf{M}_{+1} = \frac{M_0\alpha_\mathrm{m}}{2} \mathrm{diag}\left[e^{i\theta_0^{(1)}}, e^{i\theta_0^{(2)}}, e^{i\theta_0^{(3)}}\right]. \tag{C.13}$$

The stiffness matrix $\mathbf{K}(\mu)$ becomes

$$\mathbf{K}(\mu) = K \begin{bmatrix} 2 & -1 & -e^{i\mu} \\ -1 & 2 & -1 \\ -e^{-i\mu} & -1 & 2 \end{bmatrix}. \tag{C.14}$$

The assembled system matrix $\mathbf{L}_0$, $\mathbf{L}_1$, and $\mathbf{L}_2$ are derived as follows

$$\mathbf{L}_0(\mu) = \begin{bmatrix} \omega_\mathrm{m}^2 \mathbf{M}_0 - \mathbf{K}(\mu) & 0 & 0 \\ 0 & -\mathbf{K}(\mu) & 0 \\ 0 & 0 & \omega_\mathrm{m}^2 \mathbf{M}_0 - \mathbf{K}(\mu) \end{bmatrix}, \tag{C.15}$$

$$\mathbf{L}_1(\mu) = \begin{bmatrix} -2\omega_\mathrm{m}\mathbf{M}_0 & -\omega_\mathrm{m}\mathbf{M}_{-1} & 0 \\ -\omega_\mathrm{m}\mathbf{M}_{+1} & 0 & \omega_\mathrm{m}\mathbf{M}_{-1} \\ 0 & \omega_\mathrm{m}\mathbf{M}_{+1} & 2\omega_\mathrm{m}\mathbf{M}_0 \end{bmatrix}, \tag{C.16}$$

$$\mathbf{L}_2(\mu) = \begin{bmatrix} \mathbf{M}_0 & \mathbf{M}_{-1} & 0 \\ \mathbf{M}_{+1} & \mathbf{M}_0 & \mathbf{M}_{-1} \\ 0 & \mathbf{M}_{+1} & \mathbf{M}_0 \end{bmatrix}. \tag{C.17}$$

The dispersion diagram of the modulated metamaterial can be computed according to the eigenvalue Eq. (C.8), and the corresponding eigenvectors are

$$\mathbf{a}_\mathrm{total} = \left[a_{-1}^{(1)}, a_{-1}^{(2)}, a_{-1}^{(3)}, a_0^{(1)}, a_0^{(2)}, a_0^{(3)}, a_1^{(1)}, a_1^{(2)}, a_1^{(3)}\right]^T. \tag{C.18}$$

References

Bobrovnitskii, Y.I., 2013. Energy characteristics of oscillatory systems with internal (hidden) degrees of freedom. Acoust. Phys. 59, 1–5.

Casadei, F., Delpero, T., Bergamini, A., Ermanni, P., Ruzzene, M., 2012. Piezoelectric resonator arrays for tunable acoustic waveguides and metamaterials. J. Appl. Phys. 112, 064902.

Cassedy, E.S., 1967. Dispersion relations in time-space periodic media: part II-Unstable interactions. Proc. IEEE 55, 1154–1168.

Cassedy, E.S., Oliner, A.A., 1963. Dispersion relations in time-space periodic media: part I-stable interactions. Proc. IEEE 51, 1342–1359.

Chen, Y.Y., Hu, G.K., Huang, G.L., 2016. An adaptive metamaterial beam with hybrid shunting circuits for extremely broadband control of flexural waves. Smart Mater. Struct. 25, 105036.

Chen, Y.Y., Huang, G.L., Sun, C.T., 2014. Band gap control in an active elastic metamaterial with negative capacitance piezoelectric shunting. J. Vib. Acoust. 136, 061008.

Christensen, J., Kadic, M., Kraft, O., Wegener, M., 2015. Vibrant times for mechanical metamaterials. MRS Commun. 5, 453–462.

Craster, R.V., Guenneau, S., 2013. Acoustic Metamaterials: Negative Refraction, Imaging, Lensing and Cloaking. Springer.

Cummer, S.A., Christensen, J., Alù, A., 2016. Controlling sound with acoustic metamaterials. Nature Rev. Mater. 1, 16001.

Danas, K., Kankanala, S.V., Triantafyllidis, N., 2012. Experiments and modeling of iron-particle-filled magnetorheological elastomers. J. Mech. Phys. Solids 60, 120–138.

Fink, M., Cassereau, D., Derode, A., Prada, C., Roux, P., Tanter, M., Thomas, J.-L., Wu, F., 2000. Time-reversed acoustics. Rep. Prog. Phys. 63, 1933.

Fleury, R., Sounas, D.L., Haberman, M.R., Alù, A., 2015. Nonreciprocal acoustics. Acoust. Today 11, 14–21.

Fleury, R., Sounas, D.L., Sieck, C.F., Haberman, M.R., Alù, A., 2014. Sound isolation and giant linear nonreciprocity in a compact acoustic circulator. Science 343, 516–519.

Gliozzi, A.S., Miniaci, M., Krushynska, A.O., Morvan, B., Scalerandi, M., Pugno, N.M., Bosia, F. A frequency-preserving and time-invariant metamaterial-based nonlinear acoustic diode.

Gu, Z.-m., Hu, J., Liang, B., Zou, X.-y., Cheng, J.-c., 2016. Broadband non-reciprocal transmission of sound with invariant frequency. Sci. Rep. 6, 19824.

Gump, J., Finkler, I., Xia, H., Sooryakumar, R., Bresser, W.J., Boolchand, P., 2004. Light-induced giant softening of network glasses observed near the mean-field rigidity transition. Phys. Rev. Lett. 92, 245501.

Huang, H.H., Sun, C.T., 2009. Wave attenuation mechanism in an acoustic metamaterial with negative effective mass density. New J. Phys. 11, 013003.

Kherraz, N., Haumesser, L., Levassort, F., Benard, P., Morvan, B., 2016. Controlling Bragg gaps induced by electric boundary conditions in phononic piezoelectric plates. Appl. Phys. Lett. 108, 093503.

Liang, B., Guo, X.S., Tu, J., Zhang, D., Cheng, J.C., 2010. An acoustic rectifier. Nat. Mater. 9, 989–992.

Liang, B., Yuan, B., Cheng, J.-c., 2009. Acoustic diode: rectification of acoustic energy flux in one-dimensional systems. Phys. Rev. Lett. 103, 104301.

Liu, Z., Zhang, X., Mao, Y., Zhu, Y.Y., Yang, Z., Chan, C.T., Sheng, P., 2000. Locally resonant sonic materials. Science 289, 1734–1736.

Lurie, K.A., 2007. An Introduction to the Mathematical Theory of Dynamic Materials. Springer, New York, NY.

Ma, G., Sheng, P., 2016. Acoustic metamaterials: from local resonances to broad horizons. Sci. Adv. 2, e1501595.

Milton, G.W., Briane, M., Willis, J.R., 2006. On cloaking for elasticity and physical equations with a transformation invariant form. New J. Phys. 8, 248.

Milton, G.W., Mattei, O., 2017. Field patterns: a new mathematical object. Proc. R. Soc. A: Math. Phys. Eng. Sci. 473, 20160819.

Milton, G.W., Willis, J.R., 2007. On modifications of Newton's second law and linear continuum elastodynamics. Proc. R. Soc. A 463, 855–880.

Miniaci, M., Gliozzi, A.S., Morvan, B., Krushynska, A., Bosia, F., Scalerandi, M., Pugno, N.M., 2017. Proof of concept for an ultrasensitive technique to detect and localize sources of elastic nonlinearity using phononic crystals. Phys. Rev. Lett. 118, 214301.

Miniaci, M., Pal, R.K., Morvan, B., Ruzzene, M., 2018. Experimental observation of topologically protected helical edge modes in patterned elastic plates. Phys. Rev. X 8, 031074.

Mousavi, S.H., Khanikaev, A.B., Wang, Z., 2015. Topologically protected elastic waves in phononic metamaterials. Nat. Commun. 6, 8682.

Nassar, H., Chen, H., Norris, A.N., Haberman, M.R., Huang, G.L., 2017a. Non-reciprocal wave propagation in modulated elastic metamaterials. Proc. R. Soc. A: Math. Phys. Eng. Sci. 473, 20170188.

Nassar, H., Xu, X.C., Norris, A.N., Huang, G.L., 2017b. Modulated phononic crystals: Non-reciprocal wave propagation and Willis materials. J. Mech. Phys. Solids 101, 10–29.
Norris, A.N., Shuvalov, A.L., 2011. Elastic cloaking theory. Wave Motion 48, 525–538.
Popa, B.-I., Cummer, S.A., 2014. Non-reciprocal and highly nonlinear active acoustic metamaterials. Nat Commun. 5, 3398.
Reed, E.J., Soljacic, M., Joannopoulos, J.D., 2003. Reversed doppler effect in photonic crystals. Phys. Rev. Lett. 91, 133901.
Shui, L.-Q., Yue, Z.-F., Liu, Y.-S., Liu, Q.-C., Guo, J.-J., He, X.-D., 2015. Novel composites with asymmetrical elastic wave properties. Compos. Sci. Technol. 113, 19–30.
Slater, J.C., 1958. Interaction of waves in crystals. Rev. Mod. Phys. 30, 197–222.
Swinteck, N., Matsuo, S., Runge, K., Vasseur, J.O., Lucas, P., Deymier, P.A., 2015. Bulk elastic waves with unidirectional backscattering-immune topological states in a time-dependent superlattice. J. Appl. Phys. 118, 063103.
Trainiti, G., Ruzzene, M., 2016. Non-reciprocal elastic wave propagation in spatiotemporal periodic structures. New J. Phys. 18, 083047.
Vila, J., Pal, R.K., Ruzzene, M., Trainiti, G., 2017. A Bloch-based procedure for dispersion analysis of lattices with periodic time-varying properties. J. Sound Vib. 406, 363–377.
Willis, J.R., 1981. Variational principles for dynamic problems for inhomogeneous elastic media. Wave Motion 3, 1–11.
Yao, S., Zhou, X., Hu, G., 2008. Experimental study on negative effective mass in a 1D mass–spring system. New J. Phys. 10, 043020.
Zhou, X., Hu, G., 2009. Analytic model of elastic metamaterials with local resonances. Phys. Rev. B 79, 195109.
Zhou, X., Liu, X., Hu, G., 2012. Elastic metamaterials with local resonances: an overview. Theor. Appl. Mech. Lett. 2, 041001.
Zhu, X., Ramezani, H., Shi, C., Zhu, J., Zhang, X., 2014. PT-symmetric acoustics. Phys. Rev. X 4, 031042.